4598 *Chem. Mater.* **2009,** *21,* 4598–4607
DOI:10.1021/cm901658k

CHEMISTRY OF MATERIALS
Article

Controlled Synthesis of Ln^{3+} (Ln = Tb, Eu, Dy) and V^{5+} Ion-Doped YPO_4 Nano-/Microstructures with Tunable Luminescent Colors

Chunxia Li,[†] Zhiyao Hou,[†,‡] Cuimiao Zhang,[†] Piaoping Yang,[†,‡] Guogang Li,[†]
Zhenhe Xu,[†] Yong Fan,[†] and Jun Lin*[,†]

[†]*State Key Laboratory of Rare Earth Resource Utilization, Changchun Institute of Applied Chemistry, Chinese Academy of Sciences, Changchun 13002, P. R. China, and*
[‡]*College of Materials Science and Chemical Engineering, Harbin Engineering University, Harbin 150001, P. R. China*

Received June 16, 2009. Revised Manuscript Received August 20, 2009

YPO_4 nano/microcrystals with multiform crystal phases and morphologies, such as hexagonal nano/submicroprisms, spherical-like nanoparticles, and nanorods with different length/diameter ratios as well as tetragonal nanospindles, have been synthesized via a facile hydrothermal route. A series of controlled experiments indicate that the pH values in the initial solution, phosphorus sources, and the organic additive trisodium citrate (Cit^{3-}) are responsible for crystal phase and shape determination of final products. It is found that Cit^{3-} as a ligand and shape modifier has the dynamic effect by adjusting the growth rate of different facets under different experimental conditions, resulting in the formation of various geometries of the final products. The possible formation mechanisms for products with diverse architectures have been presented. More importantly, a systematic study on the photoluminescence of Ln^{3+} (Ln = Tb, Eu, Dy) and V^{5+} ion-doped samples annealed at 500 °C has been explored in order to obtain the multicolor emission in a single host lattice. The ability to generate YPO_4 nano/microstructures with diverse shapes and tunable emission colors provides a great opportunity for systematically evaluating their luminescence properties, as well as fully exploring their application in many types of color display fields.

1. Introduction

In modern chemistry and materials science, the precisely architectural manipulation of nanocrystals (NCs) with well-defined morphologies and accurately tunable sizes remains the research focus and one of the challenging issues, because it is well-known that the properties of the materials closely interrelate with geometrical factors such as shape, dimensionality, and size.[1] So far, dramatic efforts have been dedicated to develop new approaches for the fabrication of a range of inorganic crystals in different systems to enhance their performance in currently existing applications. Although a general approach to the fabrication of the nanocrystals in a precisely controlled manner is not yet available, it is widely accepted that one of the promising and popular strategies of shape and size control is to select carefully an appropriate organic additive with functional groups that selectively adheres to a particular crystal facet and effectively slower the growth of that facet relative to others, leading to the morphological modification of the crystals.[2] Among a variety of organic additives, trisodium citrate (Cit^{3-}) is one of the most common and important organic molecules that has been used extensively as the stabilizer and structure-directing agent to control the nucleation, growth and alignment of crystals.[3,4] For instances, Qian and coworkers reported the influences of Cit^{3-} on the Co nanowires[5] and doughnut-shaped ZnO microparticles.[6] In our previous researches, we have studied systematically the key roles of Cit^{3-} in tailoring the crystal phases, shapes and sizes of $NaREF_4$ (RE = Y, Yb, and Lu) and REF_3 nano/microcrystals.[7] As a continuation and extension of this work, here we will extend this method to the fabrication of YPO_4 crystals so as to test the role of Cit^{3-} in the control of crystal phases and shapes of the final products.

---

*Corresponding author. E-mail: jlin@ciac.jl.cn.

(1) (a) Alivisatos, A. P. *Science* **1996**, *271*, 933. (b) Hu, J.; Odom, T. W.; Lieber, C. M. *Acc. Chem. Res.* **1999**, *32*, 435. (c) Wang, X.; Zhuang, J.; Peng, Q.; Li, Y. D. *Nature* **2005**, *437*, 121.

(2) Yin, Y. D.; Alivisatos, A. P. *Nature* **2005**, *739*, 664.

(3) (a) Hu, J. Q.; Chen, Q.; Xie, Z. X.; Han, G. B.; Wang, R. H.; Ren, B.; Zhang, Y.; Yang, Z. L.; Tian, Z. Q. *Adv. Funct. Mater.* **2004**, *14*, 183. (b) Ji, X. H.; Song, X. N.; Li, J.; Bai, Y. B.; Yang, W. S.; Peng, X. G. *J. Am. Chem. Soc.* **2007**, *129*, 13939.

(4) Tian, Z. R.; Voigt, J. A.; Liu, J.; Mckenzie, B.; Mcdermott, M. J.; Podriguez, M. A.; Konishi, H.; Xu, H. *Nat. Mater.* **2003**, *2*, 281.

(5) Xie, Q.; Qian, Y. T.; Zhang, S. Y.; Fu, S. Q.; Yu, W. C. *Eur. J. Inorg. Chem.* **2006**, 2454.

(6) Liang, J. B.; Liu, J. W.; Xie, Q.; Bai, S.; Yu, W. C.; Qian, Y. T. *J. Phys. Chem. B* **2005**, *109*, 9463.

(7) (a) Li, C. X.; Yang, J.; Quan, Z. W.; Yang, P. P.; Kong, D. Y.; Lin, J. *Chem. Mater.* **2007**, *19*, 4933. (b) Li, C. X.; Quan, Z. W.; Yang, J.; Yang, P. P.; Lin, J. *Inorg. Chem.* **2007**, *46*, 6329. (c) Li, C. X.; Quan, Z. W.; Yang, P. P.; Yang, J.; Lian, H. Z.; Lin, J. *J. Mater. Chem.* **2008**, *18*, 1253. (d) Li, C. X.; Yang, J.; Yang, P. P.; Lian, H. Z.; Lin, J. *Chem. Mater.* **2008**, *20*, 4317.

As an important class of lanthanide inorganic compounds, rare earth orthophosphates ($REPO_4$) have been extensively applied in phosphors, laser hosts, biolabeling, and photo upconversion materials.[8] The crystal structures of rare earth orthophosphates exhibit in four polymorphs: monazite (monoclinic), rhabdophane (hexagonal), zircon (tetragonal), and churchite (monoclinic), depending on cation radii and synthesis conditions. Before we started to work on this subject, a lot of efforts had been devoted to the chemical synthesis of YPO_4 nano/microstructures, including hydro-/solvothermal method,[9] limited anion-exchange reaction,[10] coprecipitation method,[11] and so on.[12] From the perspective of application, nanomaterials are not only synthesized in large quantities with desired composition, reproducible size, shape, and structure but also prepared and assembled using green, environmentally responsible methodologies. Compared with the synthesis in the organic solvents, a water-based system should provide a relatively green chemical alternative to the preparation of various nanomaterials because it does not involve toxic organic solvents. Moreover, a water-based system also provides a number of other merits such as simplicity, safety, convenience, and the potential for large-scale production. For these reasons, the water-based systems as a more attractive route to the shape-controlled synthesis of nanomaterials have recently received more and more attention.[13] Additionally, the materials emitting multiple colors have become a research focus because of their important role in the field of light display systems, lasers and optoelectronic devices.[14] Various colors can be achieved by adjusting the relative amounts of red, green, and blue luminescent components. Among numerous fluorescence materials, the fluorescence materials activated by lanthanide ions (Ln^{3+}) have attracted extensive attention because of their wide range of emission colors and excellent luminescence properties.[15] However, to the best of our knowledge, there are no systematic accounts about the effects of Cit^{3-} on the morphological growth process of YPO_4 nano/microstructures in a water-based system and tunable luminescence properties by doping different Ln^{3+} ions hitherto.

Herein, we report the controlled synthesis and tunable luminescence properties of YPO_4 nano/microstructures in a water-based system. The purpose of our study is based on the following three aspects: (i) using Cit^{3-} as an organic additive we wish to present the exquisite control over the crystal structure, size, and shape of the products by simply changing the multiple experimental parameters; (ii) we will explore the multicolor phosphors in YPO_4 matrix through the elaborate choice of the doped Ln^{3+} ions, which is of great importance and may provide a gateway into the practical application of the materials; (iii) hydrothermal method using water as the reaction medium represents an environmentally benign and user-friendly approach.[16] Therefore, in this paper, via a facile hydrothermal route we first study the effects of solution pH, phosphorus source and organic additive Cit^{3-} on the crystal phase, size, and morphologies of products. Then we concentrate on the luminescence properties of YPO_4 phosphors with different doped Ln^{3+} ($Ln = Tb, Eu, Dy$) and V^{5+} ions in an effort to adjust the emission colors of the final products.

2. Experimental Section

Preparation. The rare earth oxides RE_2O_3 ($RE = Y, Eu, Dy$) (99.999%) and Tb_4O_7 (99.999%) were purchased from Science and Technology Parent Company of Changchun Institute of Applied Chemistry and other chemicals were purchased from Beijing Chemical Company, China. All chemicals are of analytical grade reagents and used directly without further purification. Rare earth chloride stock solutions of 0.2 M were prepared by dissolving the corresponding metal oxide in hydrochloric acid at elevated temperature. In a typical procedure, 10 mL YCl_3 (0.2 M) was added into 20 mL of aqueous solution containing 2 mmol of trisodium citrate (labeled as Cit^{3-}) to form the $Y^{3+}-Cit^{3-}$ complex (1:1 molar ratio for Cit^{3-}/Y^{3+}). After vigorous stirring for 30 min, 2 mmol of Na_3PO_4 was added into the above solution and the pH of the mixture was adjusted to about 2 by adding HCl (1 M). After additional agitation for 15 min, the as-obtained mixing solution was transferred into a Teflon bottle held in a stainless steel autoclave, sealed and maintained at 180 °C for 24 h. As the autoclave was cooled to room temperature naturally, the precipitates were separated by centrifugation, washed with deionized water and ethanol in sequence, and then dried in air at 80 °C for 12 h. The as-prepared product was denoted as **P1**. Other samples (**P2−P9**) were prepared by the similar procedure except for different phosphorus sources and pH conditions. The pH of the mixture was adjusted to a specific value by adding NaOH solution (3 M) or HCl (1 M) solution. In addition, **P10−P13** samples were prepared with different molar ratio of Cit^{3-}/Y^{3+} and other conditions are the same as those for synthesizing **P5**. The experimental conditions are summarized in Table 1. It should

---

(8) (a) Büehler, G.; Feldmann, C. *Angew. Chem., Int. Ed.* **2006**, *45*, 4864. (b) Meiser, F.; Cortez, C.; Caruso, F. *Angew. Chem., Int. Ed.* **2004**, *43*, 5954. (c) Heer, S.; Lehmann, O.; Haase, M.; Güdel, H. U. *Angew. Chem., Int. Ed.* **2003**, *42*, 3179.

(9) (a) Yan, R. X.; Sun, X. M.; Wang, X.; Peng, Q.; Li, Y. D. *Chem.—Eur. J.* **2005**, *11*, 2183. (b) Huo, Z. Y.; Chen, C.; Chu, D.; Li, H. H.; Li, Y. D. *Chem.—Eur. J.* **2007**, *13*, 7708. (c) Zhang, Y. W.; Yan, Z. G.; You, L. P.; Si, R.; Yan, C. H. *Eur. J. Inorg. Chem.* **2003**, 4099. (d) Fang, Y. P.; Xu, A. W.; Song, R. Q.; Zhang, H. X.; You, L. P.; Yu, J. C.; Liu, H. Q. *J. Am. Chem. Soc.* **2003**, *125*, 16025.

(10) Mai, H. X.; Zhang, Y. W.; Sun, L. D.; Yan, C. H. *Chem. Mater.* **2007**, *19*, 4514.

(11) Lai, H.; Bao, A.; Yang, Y. M.; Tao, Y. C.; Yang, H.; Zhang, Y.; Han, L. L. *J. Phys. Chem. C* **2008**, *112*, 282.

(12) (a) Di, W. H.; Wang, X. J.; Chen, B. J.; Lu, S. Z.; Ren, X. G. *Appl. Phys. Lett.* **2006**, *88*, 011907. (b) Di, W. H.; Wang, X. J.; Chen, B.; Lu, S. Z.; Zhao, X. X. *J. Phys. Chem. C* **2008**, *109*, 13154. (c) Huo, Z. Y.; Chen, C.; Li, Y. D. *Chem. Commun.* **2006**, 3522. (d) Nedelec, J. M.; Avignant, D.; Mahiou, R. *Chem. Mater.* **2002**, *14*, 651.

(13) Lim, B.; Jiang, M. J.; Tao, J.; Camargo, P. H. C.; Zhu, Y. M.; Xia, Y. N. *Adv. Funct. Mater.* **2008**, *18*, 1.

(14) (a) Zhao, D.; Seo, S. J.; Bae, B. S. *Adv. Mater.* **2007**, *19*, 3473. (b) Zhao, Y. S.; Fu, H. B.; Hu, F. Q.; Peng, A. D.; Yao, J. N. *Adv. Mater.* **2007**, *19*, 3554.

(15) (a) Ehlert, O.; Thomann, R.; Darbandi, M.; Nann, T. *Acs Nano* **2008**, *2*, 120. (b) Wang, F.; Liu, X. G. *J. Am. Chem. Soc.* **2008**, *130*, 5642. (c) Su, Y. G.; Li, L. P.; Li, G. S. *Chem. Commun.* **2008**, 4004. (d) Lin, C. K.; Zhang, C. M.; Lin, J. *J. Phys. Chem. C* **2007**, *111*, 3300. (e) Lin, C. K.; Luo, Y.; You, H.; Quan, Z. W.; Zhang, J.; Fang, J.; Lin, J. *Chem. Mater.* **2006**, *18*, 458. (f) Lin, C. K.; Wang, H.; Kong, D. Y.; Yu, M.; Liu, X. M.; Wang, Z. L.; Lin, J. *Eur. J. Inorg. Chem.* **2006**, 3667.

(16) (a) Mao, Y.; Wong, S. S. *J. Am. Chem. Soc.* **2006**, *128*, 8217. (b) Song, R. Q.; Xu, A. W.; Yu, S. H. *J. Am. Chem. Soc.* **2007**, *129*, 4152.

Table 1. Summary of the Experiment Conditions and the Corresponding Morphologies and Dimensions of the Samples; All Samples Were Hydrothermally Treated at 180 °C for 24 h

sample	phosphate source	Cit^{3-}:Y^{3+} molar ratio	pH	crystal phase	morphology	diameter (nm)	length (nm)
P1	Na_3PO_4	1:1	2	hexagonal and tetragonal mixture	mixture of prisms and nanocubes		
P2		1:1	6	hexagonal	hexagonal prism-like nanoparticles	120	130
P3		1:1	11	hexagonal	spherical-like nanoparticles	100	
P4	$NH_4H_2PO_4$	1:1	2	hexagonal and tetragonal mixture	ill shape		
P5		1:1	4	hexagonal	hexagonal submicroprisms	930	710
P6		1:1	11	hexagonal	submicroprism aggregates		
P7	$Na_5P_3O_{10}$	1:1	2	hexagonal and tetragonal mixture	nanorods	35	60
P8		1:1	6	hexagonal	nanorods	80	180
P9		1:1	11	hexagonal and tetragonal mixture	nanorods	200	850
P10	$NH_4H_2PO_4$	0	4	tetragonal	nanospindles	45	180
P11		2:1	4	hexagonal	hexagonal submicroprisms	300	200
P12		3:1	4	hexagonal	irregular submicroprisms	330	210
P13		4:1	4	hexagonal	hexagonal submicroprisms with concave center	200	100

be stated that all samples were hydrothermally treated at 180 °C for 24 h.

Characterization. Powers X-ray diffraction (XRD) measurements were performed on a Rigaku-Dmax 2500 diffractometer at a scanning rate of 15°/min in the 2θ range from 10 to 80°, with graphite monochromatized Cu Kα radiation (λ = 0.15405 nm). Infrared spectra were measured on a Vertex 70 FT-IR spectrophotometer (Bruker) with the KBr pellet technique. SEM micrographs were obtained using a field-emission scanning electron microscope (FE-SEM, XL30, Philips). Low- to high-resolution transmission electron microscopy (TEM) was performed using FEI Tecnai G2 S-Twin with a field-emission gun operating at 200 kV. Images were acquired digitally on a Gatan multiople CCD camera. The photoluminescence (PL) excitation and emission spectra of the as-obtained powders were recorded with a Hitachi F-4500 spectrophotometer equipped with a 150 W xenon lamp as the excitation source. The PL lifetimes of the samples were measured with a Lecroy Wave Runner 6100 Digital Oscilloscope (1 GHz) using a tunable laser (pulse width = 4 ns) as the excitation source (Continuum Sunlite OPO). All the measurements were performed at room temperature.

3. Results and Discussion

Structures. The composition and phase purity of the products were first examined by XRD. XRD patterns of the samples by using Na_3PO_4 as phosphorus source with hydrothermally treatment at 180 °C for 24 h under different pH conditions are shown in Figure 1. The diffraction peaks of the sample **P1** (Figure 1a) at pH 2 can be indexed as a mixture of hexagonal phase $YPO_4 \cdot 0.8H_2O$ (JCPDS No. 42−0082) and tetragonal YPO_4 (denoted with asterisks, JCPDS No. 11−0254). However, the hydrothermally obtained products **P2** (Figure 1b) and **P3** (Figure 1c) at pH 6 and pH 11 have a pure hexagonal phase of $YPO_4 \cdot 0.8H_2O$ with the cell parameters a = 6.833 Å and c = 6.291 Å (JCPDS No. 42−0082). No peaks of any other phases or impurities are detected. This indicates that the solution pH has a significant effect on the crystal phases of the products. If Na_3PO_4 was replaced by $NH_4H_2PO_4$ and $Na_5P_3O_{10}$ as phosphorus source, the XRD patterns of as-prepared products at different pH values are shown in Figures S1 and S2 of Supporting Information. The case using $NH_4H_2PO_4$ as P source is similar to that using Na_3PO_4 as P source. The sample obtained at pH 2 is coexistent phases, whereas the products prepared at pH 4 and pH 11 are also characteristic of a pure hexagonal phase of $YPO_4 \cdot 0.8H_2O$ (Figure S1 in the Supporting Information). In contrast, the pure hexagonal $YPO_4 \cdot 0.8H_2O$ phase can be obtained at pH 6, whereas the mixture of hexagonal and tetragonal phases can be achieved at pH 11 and pH 2 under the condition of using $Na_5P_3O_{10}$ as P source (Figure S2 in the Supporting Information). The above results suggest that the different products have different growth habits under diverse reaction conditions.

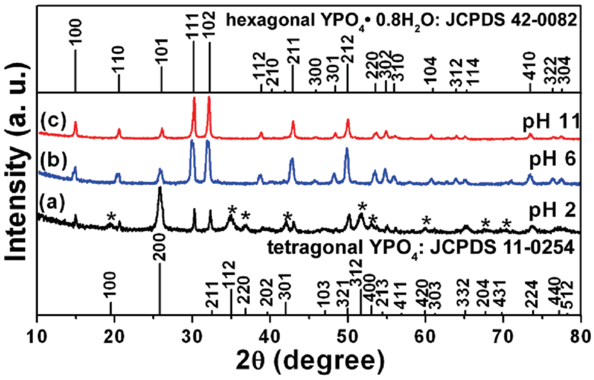

Figure 1. XRD patterns of the as-synthesized samples (**P1**−**P3**) using Na_3PO_4 as P source at different pH values: (a) pH 2, the mixture of hexagonal and tetragonal phases (* denotes as tetragonal YPO_4); (b) pH 6, hexagonal $YPO_4 \cdot 0.8H_2O$; (c) pH 11, hexagonal $YPO_4 \cdot 0.8H_2O$. The standard data of hexagonal $YPO_4 \cdot 0.8H_2O$ (JCPDS 42−0082) and tetragonal YPO_4 (JCPDS 11−0254) were used as references.

FT-IR Spectrum. To further examine the purity of $YPO_4 \cdot 0.8H_2O$ products, we performed the FT-IR spectroscopy by using sample **P2** as a representative example (see Figure S3 in the Supporting Information). It can be clearly seen that the vibration bands at 539 and 631 cm^{-1} and a broadband centered at 1085 cm^{-1} represent the characteristic adsorption of the phosphate groups. The

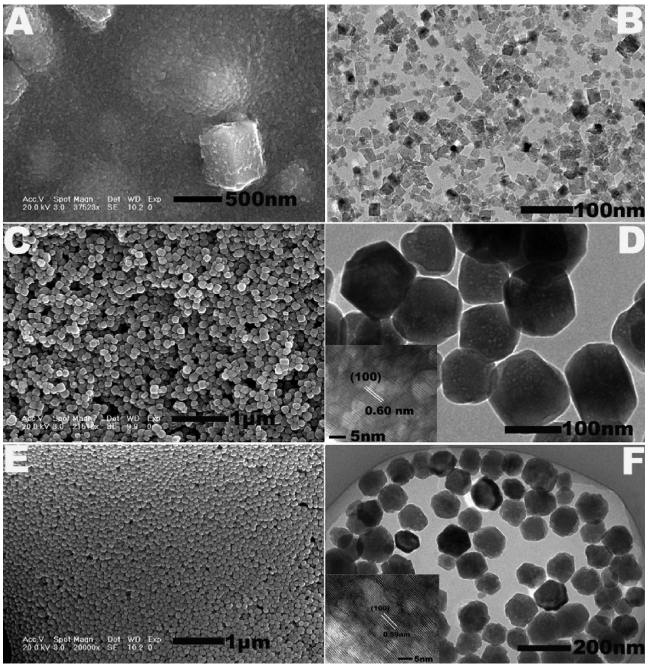

Figure 2. (A) SEM, (B) TEM, and (inset in B) HRTEM images of **P1**; (C) SEM, (D) TEM, and (inset in D) HRTEM images of **P2**; (E) SEM, (F) TEM, and (inset in F) HRTEM images of **P3**. These samples are prepared using Na_3PO_4 as P source at different pH values.

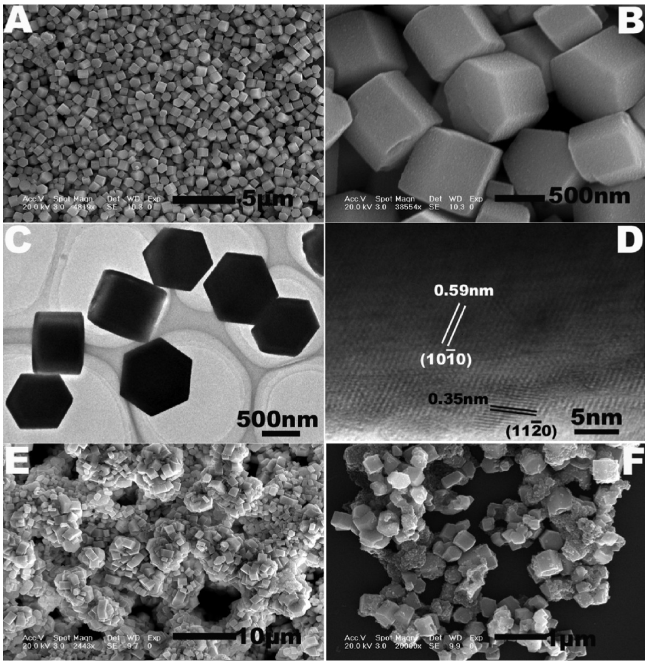

Figure 3. (A, B) SEM, (C) TEM, and (D) HRTEM images of **P5**; SEM images of (E) **P4** and (F) **P6**. These samples are prepared using $NH_4H_2PO_4$ as P source at different pH values.

peaks at 3510 and 1611 cm^{-1} should correspond to the surface-adsorbed water and hydroxyl groups, respectively.[17] The absorption bands at 2923 and 2857 cm^{-1} (υ_{CH3} and υ_{CH2}) as well as 1412 cm^{-1} (δ_{CH}) can be attributed to the characteristic frequencies of residual organic additive trisodium citrate ($Na_3C_6H_5O_7 \cdot 2H_2O$, labeled as Cit^{3-}). Although the as-prepared sample was washed several times with water and ethanol, there were still a small fraction of organic molecules Cit^{3-} on the surface of the particles.

Morphologies. The morphologies and dimensions of the products are summarized in Table 1. From Table 1, it is found that the phosphorus sources and pH values of the initial reaction solution are two categories of predominantly influencing factors in the determination of the shapes and sizes of the final products, which will be discussed in the following paragraphs.

A. Na_3PO_4 As Phosphorus Source. The SEM images provide direct information about the size and typical shapes of the as-synthesized YPO_4 samples grown under different experimental conditions. Figure 2 illustrates the representative SEM images of the samples prepared by using Na_3PO_4 as phosphorus source at different pH values. The sample **P1** is composed of the mixture of larger hexagonal prisms and smaller nanoparticles, as shown in Figure 2A. The TEM image shows that these nanoparticles have cubic shape with the average edge length of 18 nm (Figure 2B). Hydrothermal treatment of an initial solution at pH 6 results in the formation of a great deal of hexagonal nanoprisms 120 nm in diameter and 130 nm in length (**P2**), as shown in Figure 2C. However, from the TEM image (Figure 2D), one can see that the well-defined crystallographic facets of hexagonal prisms are not very evident and a small quantity of spherical-like particles can also be observed. Furthermore, the surfaces of crystals are very coarse with some smaller nanoparticles attached on them. The HRTEM image (inset in Figure 2D) shows that the as-obtained crystals are highly crystalline and that the lattice spacing is determined as ~0.60 nm corresponding to the (100) plane of $YPO_4 \cdot 0.8H_2O$. If the pH value of the initial solution is increased to 11 adjusted with NaOH (3 M), the spherical-like nanoparticles (**P3**) with high monodispersity are produced, as shown in Figure 2E. From the TEM image (Figure 2F), some regular hexagonal cross-sections can be seen that correspond to individual hexagonal prisms lying flat on the bottom face parallel to the substrate. This indicates that these spherical-like nanoparticles have a tendency to form hexagonal nanoprisms. The HRTEM image (inset in Figure 2F) further confirms the identification of hexagonal $YPO_4 \cdot 0.8H_2O$. The interplanar distance between the adjacent lattice fringes can be estimated to ~0.59 nm, which can be well indexed as *d*-spacing value of the (100) plane. These results powerfully demonstrate that even using the same phosphorus source, the different pH values of the initial reaction solution show a large impact on the crystal growth of YPO_4, and thus they influence the morphologies and microstructures of products.

B. $NH_4H_2PO_4$ As Phosphorus Source. When $NH_4H_2PO_4$ replaces Na_3PO_4 as phosphorus source under the otherwise same reaction conditions, the morphologies of the products become quite different, as shown in Figure 3.

---

(17) (a) Zhang, Q.; Yao, W. T.; Chen, X. Y.; Zhu, L. W.; Fu, Y. B.; Zhang, G. B.; Sheng, L. S.; Yu, S. H. *Cryst. Growth Des.* **2007**, *7*, 1423. (b) Soler-IIIia, G.; de, A. A.; Louis, A.; Sanchez, C. *Chem. Mater.* **2002**, *14*, 750. (c) Yu, J. M.; Zhang, L. Z.; Zheng, Z.; Zhao, J. C. *Chem. Mater.* **2003**, *15*, 2280.

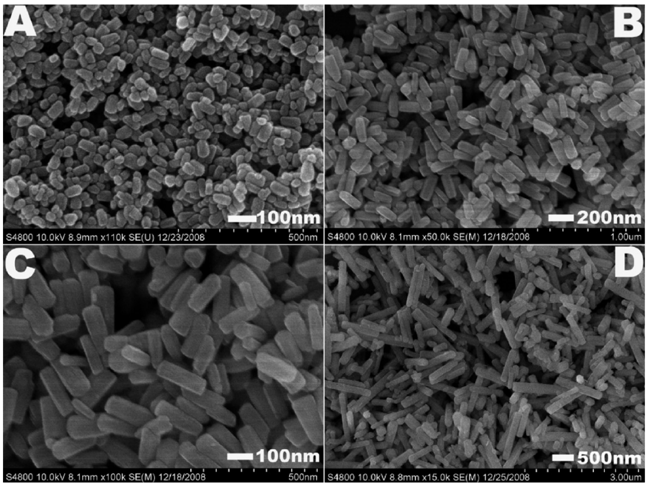

Figure 4. SEM images of as-prepared samples using $Na_5P_3O_{10}$ as P source at different pH values. (A) **P7**, (B, C) **P8**, and (D) **P9**.

If the pH value of the precursor solution is not unadjusted (pH 4), the large-scale, regular and monodisperse hexagonal submicroprisms (**P5**) with well-defined crystallographic facets become the exclusive shape, as presented in Figure 3A. Analysis of a number of the prisms shows that the diameter and length are 930 and 710 nm, respectively. The enlarged SEM image shows that the top/bottom facets and six prismatic planes are not smooth and covered with a lot of nanoparticles (Figure 3B). The observation based on a representative TEM image (Figure 3C) reveals the existence of very regular hexagonal and square cross sections, which correspond to hexagonal prisms that are perpendicular and parallel to the copper grids, respectively. The HRTEM image presents resolved fringe separations of about 0.59 and 0.35 nm, well-coincident with distances of the $(10\bar{1}0)$ and $(11\bar{2}0)$ lattice planes of hexagonal $YPO_4 \cdot 0.8H_2O$, respectively (Figure 3D). However, if the initial solution pH was changed to 2 or 11, submicroprism aggregates with flowerlike architecture (**P4**) or ill shape (**P6**) are obtained, as shown in parts E and F in Figure 3.

C. $Na_5P_3O_{10}$ As Phosphorus Source. Except for the use of Na_3PO_4 and $NH_4H_2PO_4$ as phosphorus sources, we also investigate the effects of polyphosphate $Na_5P_3O_{10}$ as phosphorus source on the morphologies of the products. Figure 4 depicts the shape evolution of the corresponding products (**P7**−**P9**) at different pH values. It can be seen clearly that these three samples all adopt nanorod shape. Furthermore, with the rise of pH value from 2 to 11, the corresponding aspect ratio of L/D (length/diameter) increases from 1.7 to 4.3. In addition, more careful observation shows that the top/bottom surfaces of these nanorods possess regular hexagonal cross-sections. Therefore, this shape can be defined as hexagonal nanorod.

Role of Organic Additive Cit^{3-}. From the morphological evolutions discussed above, we can conclude that the samples obtained with the assistance of Cit^{3-} exist primarily in the form of hexagonally shaped architectures, such as hexagonal nanoprisms, submicroprisms and nanorods with different sizes, independent of the phosphorus source used. Furthermore, it is found that organic additive Cit^{3-} has important influence on the crystal phase and morphologies in our current synthesis. By taking $NH_4H_2PO_4$ as phosphorus source for example and keeping other parameters unchanged, a comparative experiment was carried out in the absence of Cit^{3-}. Unexpectedly, the sample (**P10**) belongs to the tetragonal structure of YPO_4 dehydrated (space group: $I4_1/amd$), which is well accordant with the standard literature data (JCPDS 11−0254), as shown in Figure S4 (Supporting Information). The corresponding product takes shape of uniform nanospindles instead of hexagonal submicroprisms (Figure 5A). The mean diameter and length of these nanospindles are 45 and 180 nm, respectively. A typical TEM image of the sample is presented in Figure 5B, in which plenty of nanospindles with a narrow size distribution can be observed clearly. The corresponding HRTEM image displays the interplanar distances of 0.35 nm, ascribed to the lattice spacing of the (200) planes of tetragonal YPO_4, suggesting [001] to be the preferred growth direction for YPO_4 nanospindles (inset in Figure 5B). The switches of the crystal phases and shapes with and without Cit^{3-} should be caused by the synergic action of both the different intrinsic structure features of different YPO_4 crystallographic phases and organic additive Cit^{3-}. On the one hand, it is known that phase control is crucially important during the crystal growth process, because the properties of the materials are determined first by their phase. Furthermore, the phases of the crystalline seeds can induce different growth kinetics (isotropically or anisotropically) of the crystals due to their characteristic unit cell structures, subsequently determine the product shapes.[18]

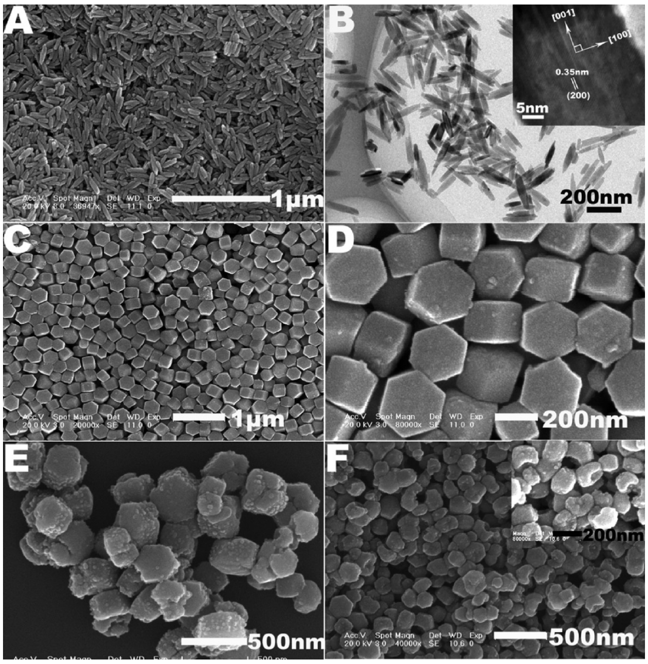

Figure 5. Morphologies for the samples (**P10**−**P13**) prepared with different molar ratios of Cit^{3-}:Y^{3+} using $NH_4H_2PO_4$ as phosphorus source. (A, B) 0 (without Cit^{3-}), (C, D) 2:1, (E) 3:1, (F) 4:1.

---

(18) Jun, Y. -W.; Choi, J.-S.; Cheon, J. *Agnew. Chem., Int. Ed.* **2006**, *45*, 3414.

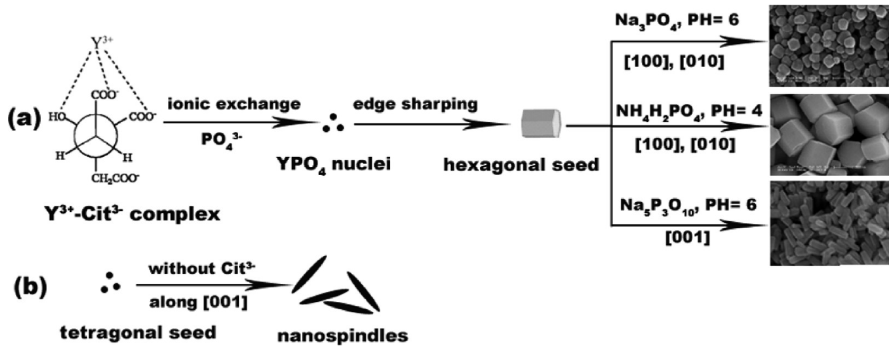

Scheme 1. Schematic Illustration for the Possible Formation Mechanism of YPO_4 with Various Morphologies Prepared in the (a) Presence and (b) Absence of Cit^{3-}

In our current system, it is evident that hex-structures of $YPO_4 \cdot 0.8H_2O$ correlate to the hexagonal phase crystal structures, whereas YPO_4 with a tetragonal phase seems to show a tendency to grow along a certain direction ([001]), leading to the formation of anisotropic 1D nanospindles. This is in very good agreement with HRTEM result (inset in Figure 5B). Although Fang et al.[9d] have pointed out that tetragonal $LnPO_4$ has no anisotropic nature, the intrinsic anisotropic feature of tetragonal $LnPO_4$ may be magnified by modifying the composition of the solution under appropriate synthetic conditions such that 1D nanostructures are achieved.[19] On the other hand, organic additive Cit^{3-} plays a key role in the transformation of crystal phases and shapes of the final products. In a solution-phase synthesis, organic additives acting as surfactants or capping agents can change the order of free energies of different facets through their interaction with metal surface. This alteration may significantly affect the relative growth rates of different facets.[20] In our case, Cit^{3-} is a kind of organic ligand with three carboxylate groups, which can form $Y^{3+}-Cit^{3-}$ complexes with Y^{3+} ions through stronger coordination interaction. According to LaMer's model, the formation of such complexes could control the concentration of free Y^{3+} ion concentration in solution, and thus help to control the nucleation and growth of the crystals in the view of dynamic process.[21] Then under the hydrothermal conditions the chelating of $Y^{3+}-Cit^{3-}$ complexes would be weakened and an anion-exchange reaction between PO_4^{3-} and Cit^{3-} would take place. This competition reaction gives rise to the formation of YPO_4 nuclei. During the subsequent crystal stage, because of the selective adsorption of Cit^{3-}, the growth along [001] orientation is inhibited to some degree and that of the growth sideways along [100] and [010] directions are enhanced relatively, resulting in the formation of hex-structures with more well-defined faces. It is worth noting that because of the usage of different parameters such as phosphorus source and pH value, the growth environment of the crystals are different, so the selective adsorption of Cit^{3-} on the different facets of growing YPO_4 crystallites, resulting in that the relative growth rates of YPO_4 along the [001] versus [100] directions are different. As a consequence, the products achieved under the different experimental conditions take a wealth of shapes of hex-structures such as hexagonal nanoprisms, submicroprisms, and nanorods with different aspect ratios. The whole formation mechanisms of different products are presented in Scheme 1.

From the above results, it is apparent that the cooperative action of the inherent structure features of different YPO_4 crystal phases and organic additive Cit^{3-} leads to the variation of the crystal phases and shapes of the products in both the absence and presence of Cit^{3-}. It is clear that Cit^{3-} plays double roles as a strong chelating ligand to form a stable complex with Y^{3+} and as a structure-directing reagent binding to the surface of crystals, which directly affects the growth of different crystal facets and crystallinity of the products. Similar phenomenon has been reported by Mai and co-workers, in which $REPO_4$ nanocrystals with different crystal phase (monoclinic and tetragonal) and shapes (nanowire and nanopolyhedra) can be obtained by altering the ratio of oleic acid/oleylamine.[10]

In addition, we also conducted a series of parallel experiments to further substantiate the role of Cit^{3-} in the shape control of products by altering its contents. Table S1 lists the change in morphology and particle size for $YPO_4 \cdot 0.8H_2O$ samples (**P11**−**P13**) prepared with the different molar ratios of Cit^{3-}:Y^{3+}. At the 1:1 molar ratio of Cit^{3-}:Y^{3+}, the as-prepared product (**P5**) with hexagonal structure is composed of regular and well-defined hexagonal submicroprisms (Figure 3A−C), as stated above. When the Cit^{3-}:Y^{3+} molar ratio increases to 2:1, the product (**P11**) has no noticeable morphological change except for the decrease of the sizes to 300 nm in diameter and 200 nm in length (Figure 5C) compared with that prepared with 1:1 Cit^{3-}:Y^{3+}. Furthermore, all the surfaces of crystals are very coarse with some nanoparticles attached on them (Figure 5D). However, when the ratio reaches 3:1, the irregular submicroprismatically shaped crystals (**P12**) with size of 330 nm in diameter and 210 nm in length are viewed from Figure 5E. At the higher ratio of 4:1, the as-prepared sample (**P13**) takes on more irregular morphology with concave centers (Figure 5F). It can be calculated that the average diameter of the particles is about 200 nm and the length is about

---

(19) Wang, X.; Li, Y. D. *Inorg. Chem.* **2006**, *45*, 7522.
(20) Tao, A. R.; Habas, S.; Yang, P. D. *Small* **2008**, *4*, 310.
(21) Li, Z. Q.; Zhang, Y. *Angew. Chem., Int. Ed.* **2006**, *45*, 7732.

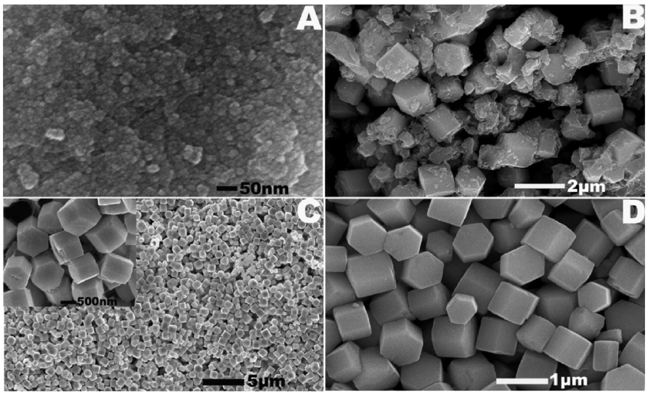

Figure 6. SEM images for $YPO_4 \cdot 0.8H_2O$ samples under similar conditions for synthesizing **P5** as a function of reaction time of (A) 1.5, (B) 3, (C) 7.5, and (D) 24 h.

100 nm. On the basis of above analysis, it can be concluded that the optimal molar ratio of Cit^{3-}:Y^{3+} for the formation of uniform $YPO_4 \cdot 0.8H_2O$ hexagonal prisms is 1:1 or 2:1.

Effect of Reaction Time: Formation Process. The morphologies of the samples were carefully investigated by quenching the reaction at different time intervals. Note that the crystal phase of $YPO_4 \cdot 0.8H_2O$ products obtained under the similar conditions for synthesizing **P5** still retains the hexagonal structure at different reaction time, as shown in Figure S5 (Supporting Information). Furthermore, the intensity of diffraction peaks increases with the extended reaction time, indicating that the crystalline degree of the samples becomes higher and higher. Figure 6 shows the SEM images of the corresponding intermediates. At t = 1.5 h, nearly spherical-like nanoparticles (Figure 6A) with a mean diameter of about 20 nm are obtained. The particle edge sharpening then occurs concomitantly with particle growth. With the reaction proceeding 3 h, the regular and well-defined submicroprisms begin to appear. However, these submicroprisms seem to be surrounded by a lot of aggregate species (Figure 6B). After 7.5 h of growth, the dominant morphology of the products is complete hexagonal submicroprism with an average diameter of 600 nm and a length of 550 nm, and the nanoparticles have been gradually consumed as shown in Figure 6C. More careful examination of the enlarged SEM image (inset in Figure 6C) indicates that these prisms are intertwisted by a large quantity of cobweblike nanowires. On aging for longer period up to 24 h, the spider cobweblike nanowires disappear completely and the submicroprisms finally grow up and separate from each other (Figure 6D). Moreover, the size of particles augment significantly (930 nm in diameter and 710 nm in height), indicating that the transversal and longitudinal growth of the crystals with the reaction time.

Synthesis of Other $REPO_4 \cdot nH_2O$ (RE = Pr, Eu, Gd, Tb, Dy, and Ho) Nanostructures. Using the similar conditions for synthesizing **P5**, we also fabricate other rare earth orthophosphate. It is necessary to point out that as-obtained products all belong to the hexagonal structures of $LnPO_4 \cdot nH_2O$, as shown in the corresponding XRD patterns (see Figure S6 in the Supporting Information). It is very interesting that only $HoPO_4 \cdot 2H_2O$ has similar shape of hexagonal submicroprisms with $YPO_4 \cdot 0.8H_2O$ (see Figure S7F in the Supporting Information), whereas other lanthanide phosphates hydrate derived under identical synthesis conditions take completely different shape. The as-obtained $PrPO_4 \cdot H_2O$ is mainly composed of well-separated elongated nanoparticles (Figure S7A). However, the morphologies of $EuPO_4 \cdot H_2O$ and $GdPO_4 \cdot H_2O$ samples are nanorods, which are constructed from the self-assembly of many even smaller nanoparticles (see Figure S7B, C in the Supporting Information). For $TbPO_4 \cdot H_2O$ and $DyPO_4 \cdot 1.5H_2O$, their shapes are 1D bundles like carrots, which consist of individual parallel nanowires (see Figure S7D, E in the Supporting Information). Although the exact reason for this phenomenon is not yet clearly known, the switches of shapes seem to be closely related to the gradual contraction of the RE^{3+} ionic radius. As a result, the physical and chemical properties change correspondingly. Previous studies on the lanthanide hydroxides, phosphates, and fluorides also indicate that the crystal structures and morphologies change gradually with decreasing ionic radii.[22,9]

Photoluminescence Properties of Ln^{3+} (Ln = Tb, Eu, Dy), V^{5+}-Doped YPO_4. It is noted that all Ln^{3+} (or V^{5+}) -doped $YPO_4 \cdot 0.8H_2O$ (hexagonal phase) or YPO_4 (tetragonal phase) samples could be prepared in the similar procedure for synthesizing **P5** or **P10**. All the doping ratios of Ln^{3+} are molar in our experiments. What's more, neither the crystal phases nor the morphologies of the products are altered. Additionally, all the samples are annealed at 500 °C for 4 h in order to improve their luminescent intensities.

Eu^{3+}-Doped Yttrium Orthophosphate with Different Crystal Phases. We first investigate the optical properties of 5 mol % Eu^{3+}-doped $YPO_4 \cdot 0.8H_2O$ submicroprisms with hexagonal structure (**P5**) and YPO_4 nanospindles with tetragonal structure (**P10**) after calcination. Their room-temperature photoluminescence spectra are shown in Figure 7 under the same measurement conditions. The excitation spectra (black line) of two samples consist of a broadband caused by the oxygen-to-europium charge transfer band (CTB) and a group of shape lines arising from the f−f transition within the Eu^{3+} $4f^6$ electron configuration. By a comparison of the two excitation spectra, one the one hand, it can be clearly seen that the position of CTB for **P10** with tetragonal structure shows obvious blue shift with respect to that for **P5** with hexagonal structure, as marked with dot lines. It is well-known that the CTB position depends on the Eu−O bond length: the longer the Eu−O bond length, the longer wavelength of the CTB.[10] Therefore, the average Eu−O bond instance in **P5** is somewhat longer than **P10.** On the other hand, the relative intensity of CTB and the strongest transition of Eu^{3+} (397 nm) are different in two samples, namely, the absorption of Eu^{3+} in **P5** is very strong,

---

[22] (a) Wang, X.; Li, Y. D. *Angew. Chem., Int. Ed.* **2002**, *41*, 4790. (b) Wang, X.; Zhuang, J.; Peng, Q.; Li, Y. D. *Inorg. Chem.* **2006**, *45*, 6661.

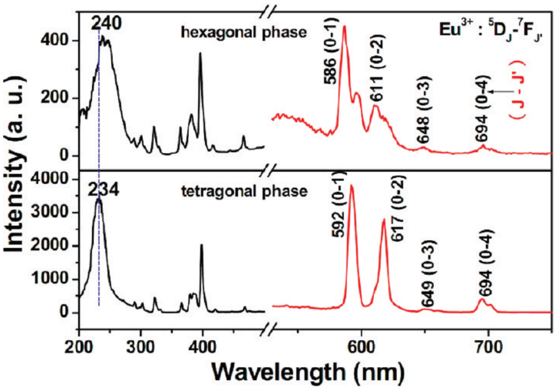

Figure 7. Room-temperature PL excitation (black line) and emission (red line) spectra of 5 mol % Eu^{3+}-doped $YPO_4 \cdot 0.8H_2O$ with hexagonal structure (**P5**) and YPO_4 with tetragonal structure (**P10**) annealed at 500 °C for 4 h.

whereas that in **P10** is very weak, suggesting the energy transfer from Eu−O CT states to 4f levels of Eu^{3+} in the latter is much more efficient than that in the former. The emission spectra (red line) are composed of $^5D_0 \rightarrow {}^7F_J$ (J = 1, 2, 3, 4) emission lines of Eu^{3+}, with the magnetic-dipole (MD) transition $^5D_0 \rightarrow {}^7F_1$ orange emission being the most prominent group. No emission from the higher energy levels ($^5D_1$, $^5D_2$) of Eu^{3+} is detected because of multiphonon relaxation based on the vibration of phosphate groups (1078 cm^{-1}).[23] Furthermore, the relative intensity of emission spectrum of **P10** is eight times as high as that of **P5**. We think that the reasons responsible for the difference of luminescence relative intensities should have three aspects. First, the distortion and covalence degree of the Eu^{3+} site are different because of their different crystal phase. Thanks to the "point site symmetry probe" character of Eu^{3+}, its optical spectra provide important information about the environment in a given host, in terms of symmetry and covalence of bonds to the ligands. So by checking the variation of the intensity ratio of the induced electron-dipole (ED) $^5D_0 \rightarrow {}^7F_2$ to the MD $^5D_0 \rightarrow {}^7F_1$ emissions, $I_{ED/MD}$, related to the Judd-Ofelt parameter Ω_2, we can derive an assessment of the distortion and covalence degree of the Eu^{3+} site.[24] In our case, it is calculated that the intensity ratio of $^5D_0 \rightarrow {}^7F_2/{}^5D_0 \rightarrow {}^7F_1$ ($I_{ED/MD}$) is 0.51 for the hexagonal phase, whereas it reaches a value of 0.78 for the tetragonal one, which reveals a higher distortion and/or higher covalence in bonds to oxygens surrounding Eu^{3+} in the YPO_4 tetragonal structure with regard to the hexagonal one. This brings on the variation of the performance of materials. Second, the difference in their morphologies and sizes is another important factor in affecting the luminescence properties, as reported previously.[25] The sample **P5** has submicroprismatic shape in diameter of 930 nm and length of 710 nm, whereas the sample **P10** has nanospindle shape in diameter of 45 nm and length of 180 nm, respectively. Different sizes and shapes result in different combinations between the surface and the adsorbed species so as to produce different quenching abilities of the emissions of the Eu^{3+} ions, which further influences the emission intensities. Finally, as is known, OH^- ions covered on the surfaces of the phosphors are a kind of very efficient quenchers of the luminescence of Ln^{3+} through multiphonon relaxation. So the existence of hydrates in the hexagonal $YPO_4 \cdot 0.8H_2O$ will affect unavoidably the emission intensity of the sample **P5** hydrated with respect to **P10** dehydrated. To sum up, the crystal structure, shape, and size as well as the OH^- ions covered on the surfaces of the phosphors account for the difference of the luminescence properties of Eu^{3+}-doped hexagonal and tetragonal YPO_4 products.

$YPO_4 \cdot 0.8H_2O$:Tb^{3+} with Different Shapes. Figure 8 depicts the excitation and emission spectra of diverse shaped $YPO_4 \cdot 0.8H_2O$: 5 mol % Tb^{3+} (**P2**, **P5**, and **P8**) obtained using different phosphorus source and measured at the same conditions. The excitation spectrum (black line) consists of a very strong broadband due to $4f^8$−$4f^7 5d$ transition of Tb^{3+} and some weak lines assigned to the characteristic f-f transition lines within Tb^{3+} $4f^8$ configuration. Moreover, the position of $4f^8$−$4f^7 5d$ transition slightly changes for the three samples. Excitation into the $4f^8$−$4f^7 5d$ transition band yields the emission spectra (green line) that have similar profiles and exhibit four obvious lines centered at 489, 542, 583, and 620 nm, originating from the transitions from the $^5D_4$ excited state to the ^7F_J (J = 6, 5, 4, 3) ground states of Tb^{3+} ion, respectively, with $^5D_4 \rightarrow {}^7F_5$ transition at 542 nm as the most prominent group. Under identical measurement conditions, the relative intensities of three samples are different, namely, the nanorod particles (**P8**) have the highest relative emission intensity, whereas the submiroprism ones (**P2**) show the lowest intensity, and the relative intensity of the former is 3 times as high as that of the latter, as shown in Figure S8 (see the Supporting Information). We ascribe the difference of luminescence relative intensities to the different morphologies and sizes of the three samples. The reasons might be as follows. First, although the different phosphorus sources are used, the crystal phase of the three products is the same, i.e., hexagonal $YPO_4 \cdot 0.8H_2O$. Second, all three samples were all treated hydrothermally at 180 °C for 24 h. Third, the precipitates have been washed with deionized water and ethanol in sequence by centrifugation-redispersion process, so there is no existence of residual Na_3PO_4, $NH_4H_2PO_4$, and $Na_5P_3O_{10}$ in the solid products. On the basis of the above analyses, it is reasonable to believe that the different luminescence properties of the products arise from their morphologies and sizes. But at this stage, it cannot be fully understood that why $YPO_4 \cdot 0.8H_2O$: 5 mol % Tb^{3+} with nanorod morphology shows higher emission intensity than those with other morphologies.

---

(23) Yu, M.; Lin, J.; Fu, J.; Zhang, H. J.; Han, Y. C. *J. Mater. Chem.* **2003**, *13*, 1413.

(24) Cascales, C.; de Andrés, A.; Sánchez-Benitez, J. *J. Phys. Chem. A* **2008**, *112*, 1464.

(25) (a) Mai, H. X.; Zhang, Y. W.; Sun, L. D.; Yan, C. H. *Chem. Mater.* **2007**, *19*, 4514. (b) Wu, X. C.; Tao, Y. R.; Song, C. Y.; Mao, C. J.; Dong, L.; Zhu, J. J. *J Phys. Chem. B* **2006**, *110*, 15791. (c) Kim, F.; Connor, S.; Song, H.; Kuykendall, T.; Yang, P. D. *Angew. Chem., Int. Ed.* **2004**, *43*, 3673. (d) Zhou, H. J.; Mao, Y. B.; Wong, S. S. *J. Mater. Chem.* **2007**, *17*, 1707.

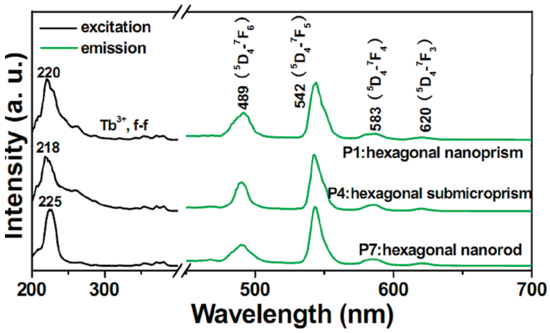

Figure 8. Room-temperature PL excitation (blank line) and emission (green line) spectra of 5 mol % Tb^{3+}-doped $YPO_4 \cdot 0.8H_2O$ samples (**P2**, **P5**, and **P8**) with different shapes annealed at 500 °C for 4 h.

Simultaneously, the PL decay curves (Figure S9, Supporting Information) for the luminescence of Tb^{3+} in **P2**, **P5**, and **P8** can further substantiate above result. These curves can be well fitted by a single exponential function as $I(t) = I_0\exp(-t/\tau)$ (I_0 is the initial emission intensity at $t = 0$ and τ is the $1/e$ lifetime of the emission center), and the lifetimes for $^5D_4$ (detected at 544 nm for $^5D_4 \rightarrow {}^7F_5$ transition) of Tb^{3+} were determined to be 2.88 (**P2**, nanoprisms), 1.92 (**P5**, submicroprisms) and 3.78 ms (**P8**, nanorods), as shown in parts a, b, and c in Figure S9 in the Supporting Information, respectively. The difference of decay lifetime further validates the difference of the emission intensities for three samples. These observations show that the size and shape are strongly related to the luminescent properties of a material.

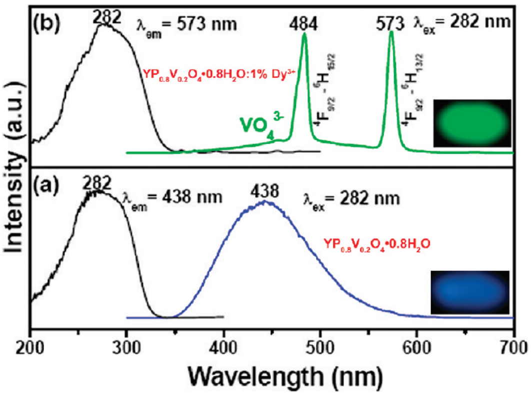

Figure 9. Room-temperature PL excitation and emission spectra of (a) $YP_{0.8}V_{0.2}O_4 \cdot 0.8H_2O$ and (b) $YP_{0.8}V_{0.2}O_4 \cdot 0.8H_2O$: 1 mol % Dy^{3+}. The insets show the corresponding luminescence photographs of the samples under short UV excitation.

$Y(P, V)O_4 \cdot 0.8H_2O$:Dy^{3+}. In our experiments, the as-obtained $YPO_4 \cdot 0.8H_2O$:1 mol % Dy^{3+} shows too weak luminescence to be detected. So we attempt to improve the luminescent properties of products by partial replacement of PO_4^{3-} ions with VO_4^{3-} ions, because the phosphate–vanadate phosphors $Y(P,V)O_4$ are more stable and have better high-temperature luminescent properties compared with pure phosphate or vanadate phosphors.[26] Additionally, the emission colors of Ln^{3+} doped $Y(P, V)O_4$ can be easily modulated by single-wavelength excitation.[27] In our experiments, the contents of PO_4^{3-} ions with respect to VO_4^{3-} have important effect on the morphology of the final products. For $YP_xV_{1-x}O_4$, only the regular shape can be achieved under the conditions of $x \geq 0.8$. Obviously, the lower content of VO_4^{3-} is favorable to form a homologous series of mixed crystals. Moreover, a small quantity of VO_4^{3-} is unable to change the hexagonal phase of the products. Figure S10 (see the Supporting Information) shows the typical SEM images of $YP_{0.8}V_{0.2}O_4 \cdot 0.8H_2O$:1 mol % Dy^{3+}. The product consists of a great deal of uniform and regular hexagonal submicroplates with very narrow size distribution (Figure S10A in the Supporting Information). The diameter and thickness of the submicroplates are 450 and 130 nm, respectively. Furthermore, the surfaces of the plates are covered with a lot of smaller nanoparticles, as portrayed in Figure S10B in the Supporting Information. Figure 9 shows the excitation and emission spectra of $YP_{0.8}V_{0.2}O_4 \cdot 0.8H_2O$ (a) and $YP_{0.8}V_{0.2}O_4 \cdot 0.8H_2O$:1 mol % Dy^{3+} (b) submicroplates annealed at 500 °C for 4 h. The excitation spectrum of $YP_{0.8}V_{0.2}O_4 \cdot 0.8H_2O$ is composed of an intense broadband centered at 282 nm, which can be assigned to the charge transfer within the VO_4^{3-} groups (black line in Figure 9a). Upon excitation at 282 nm, the emission spectrum is also a broadband centered at approximately 438 nm (blue line in Figure 9a) with a blue color under short UV excitation (inset in Figure 9a). The excitation spectrum (black line in Figure 9b) of $YP_{0.8}V_{0.2}O_4 \cdot 0.8H_2O$:1 mol % Dy^{3+} consists of strong bands with a maximum at 282 nm due to the VO_4^{3-} group and some weak lines in the longer wavelength region due to the f–f transitions of Dy^{3+} within its $4f^9$ configuration. The emission spectrum of $YP_{0.8}V_{0.2}O_4 \cdot 0.8H_2O$:1 mol % Dy^{3+} contains two parts, a broadband from 350 to 460 nm with a maximum around 450 nm and two narrow bands with maximum at 484 and 573 nm. Obviously, the former is due to the emission from the VO_4^{3-} groups of the host lattices, and the latter is due to the transitions from $^4F_{9/2}$ to $^6H_{15/2}$, $^6H_{13/2}$ of Dy^{3+}, respectively. The $YP_{0.8}V_{0.2}O_4 \cdot 0.8H_2O$:1 mol % Dy^{3+} emits bright green under the excitation of 254 nm with an UV lamp (inset in Figure 9b). The above discuss indicates that excitation energy cannot be transferred via phosphate groups in $Y(P,V)O_4$:Dy^{3+} and the energy transfer to Dy^{3+} takes place predominately from nearest vanadate neighbors.[28] The P atom possesses higher electronegativity than the V atom, and the substitution of P by V will influence the property of ion bond in $YP_xV_{1-x}O_4$ host.[29] So the introduction of VO_4^{3-} in YPO_4 host brings about great changes for the luminescent properties of Dy^{3+}.

In conclusion, the emission colors of the products can be fine-tuned by doping Ln^{3+} and V^{5+} ions. Figure S11

---

(26) (a) Blasse, G.; Grabmaier, B. C. *Luminescent Materials*; Springer: Berlin, 1994.(b) Yu, M.; Lin, J.; Wang, S. B. *Apply. Phys. A* **2005**, *80*, 353.

(27) (a) Wang, F.; Xue, X. J.; Liu, X. G. *Angew. Chem., Int. Ed.* **2008**, *47*, 906. (b) Hou, Z. Y.; Yang, P. P.; Li, C. X.; Wang, L. L.; Lian, H. Z.; Lin, J. *Chem. Mater.* **2008**, *20*, 6686.

(28) Yu, M.; Lin, J.; Zhou, Y. H.; Pang, M. L.; Han, X. M.; Wang, S. B. *Thin Solid Films* **2003**, *444*, 245.

(29) Xiao, X. Z.; Yan, B.; Song, Y. S. *Cryst. Growth Des.* **2009**, *9*, 136.

(see the Supporting Information) shows the luminescence photographs of $YPO_4 \cdot 0.8H_2O$:5 mol % Tb^{3+} (a), $YPO_4 \cdot 0.8H_2O$:5 mol % Eu^{3+} (b), $YP_{0.8}V_{0.2}O_4 \cdot 0.8H_2O$ (c) and $YP_{0.8}V_{0.2}O_4 \cdot 0.8H_2O$:1 mol % Dy^{3+} (d) upon excitation with 254 nm from a UV lamp, in which multicolors including blue, green and red can be realized.

4. Conclusions

In summary, we have demonstrated a simple and mild hydrothermal method for the synthesis of YPO_4 nano/submicrocrystals with a broad range of shapes. A series of controlled experiments show that the external factors such as solution pH values, phosphorus sources and organic additive Cit^{3-} in conjunction with intrinsic crystallographically structure of YPO_4 crystals account for the shape evolutions of the final products. More importantly, the photoluminescence properties for Ln^{3+} (Ln = Tb, Eu, Dy) and V^{5+} ions doped/codoped samples have been investigated in detail. For 5 mol % Eu^{3+}-doped samples with different crystal phases of hexagonal and tetragonal structure, not only do the positions of the CTB bands vary significantly but the intensity patterns of emission peaks are also very different. At the same time, 5 mol % Tb^{3+}-doped $YPO_4 \cdot 0.8H_2O$ samples with different shapes show different relative emission intensities. These findings indicate that the luminescence properties of a material are strongly related to its crystal structure, the shape, and size. Additionally, the luminescent properties for $YP_{0.8}V_{0.2}O_4 \cdot 0.8H_2O$: 1 mol % Dy^{3+} change greatly when the $PO_4{}^{3-}$ ions are partly replaced with $VO_4{}^{3-}$. So the fluorescence colors of the products can be tuned conveniently by the adjustment of Ln^{3+} and V^{5+} doping species. This merit of multicolor emissions in the visible region endows this kind of materials with potential application in the field of light display systems, lasers, and optoelectronic devices.

Acknowledgment. This project is financially supported by National Basic Research Program of China (2007CB935502, 2010CB327704) and the National Natural Science Foundation of China (NSFC 50702057, 50872131).

Supporting Information Available: XRD patterns of the as-synthesized samples (**P4**–**P6**) using $NH_4H_2PO_4$ as P source at different pH values (Figure S1); XRD patterns of the as-synthesized samples (**P7**–**P9**) using $Na_5P_3O_{10}$ as P source at different pH values (Figure S2); FT-IR spectrum of as-prepared $YPO_4 \cdot 0.8H_2O$ sample (**P2**) (Figure S3); XRD pattern of YPO_4 sample (**P10**) with tetragonal structure prepared in the absence of Cit^{3-} ($NH_4H_2PO_4$ as P source) (Figure S4); XRD patterns of the as-synthesized $YPO_4 \cdot 0.8H_2O$ samples under the similar conditions for synthesizing **P5** as a function of reaction time (Figure S5); XRD patterns (Figure S6) and SEM images (Figure S7) of the other $LnPO_4 \cdot nH_2O$ samples with hexagonal structure under the similar conditions for synthesizing **P5**; room-temperature PL emission spectra (λ_{ex} = 220 nm) (Figure S8) and the decay curves (Figure S9) of Tb^{3+} in 5 mol % Tb^{3+}-doped $YPO_4 \cdot 0.8H_2O$ samples (**P2**, **P5**, and **P8**) with different shapes; SEM images of $YP_{0.8}V_{0.2}O_4 \cdot 0.8H_2O$: 1 mol % Dy^{3+} (Figure S10); and luminescence photographs of $YPO_4 \cdot 0.8H_2O$:5 mol % Tb^{3+}, $YPO_4 \cdot 0.8H_2O$:5 mol % Eu^{3+}, $YP_{0.8}V_{0.2}O_4 \cdot 0.8H_2O$, and $YP_{0.8}V_{0.2}O_4 \cdot 0.8H_2O$:1 mol % Dy^{3+} upon excitation with 254 nm from a UV lamp (Figure S11) (PDF). This material is available free of charge via the Internet at http://pubs.acs.org.